Monte Carlo Study of X-Ray Detection Configurations for Benchtop X-Ray Fluorescence Computed Tomography of Gold Nanoparticle-loaded Objects

Hem Moktan[1], **Md Foiez Ahmed**[1], **Sandun Jayarathna**[1], **Luzhen Deng**[1], **Sang Hyun Cho**[1,2,*]

[1]Department of Radiation Physics, The University of Texas MD Anderson Cancer Center, Houston, TX 77030, USA

[2]Department of Imaging Physics, The University of Texas MD Anderson Cancer Center, Houston, TX 77030, USA

Abstract

Over the last decade, the performance of benchtop x-ray fluorescence computed tomography (XFCT) systems has been significantly enhanced through hardware and software optimizations. Recent studies have indicated the need of energy-resolving pixelated/array detectors in the x-ray detection component to further improve the sensitivity and image resolution of benchtop XFCT systems while meeting the realistic constraints of dose and scan time. Thus, it is of immediate interest in the research community to conduct the following investigations: a) delineation of strengths/weaknesses of detection configurations that incorporate pixelated/array detectors in combination with two most frequently used (parallel-hole and pinhole) collimators; b) one-to-one comparison of their performance under identical imaging conditions of benchtop XFCT. In this study, we developed a Geant4-based Monte Carlo model to investigate the effects of the aforementioned detection configurations on the sensitivity and image resolution of a benchtop XFCT system. Using this model, we simulated the detection of x-ray fluorescence and scattered photons from gold nanoparticle-containing phantoms using energy-resolving pixelated detectors coupled with parallel-hole and pinhole collimators. Simulation results demonstrated that the detector consisting of large pixels (1 mm x 1 mm) combined with a parallel-hole collimator had better sensitivity (i.e., lower detection limit) than the detector made of smaller pixels (0.25 mm x 0.25 mm) coupled with a pinhole collimator. In comparison, although slightly less sensitive, the latter detector configuration achieved better image resolution than did the former. Thus, a detection configuration consisting of a pixelated detector with submillimeter pixels and a pinhole collimator is preferable when image resolution is critical for benchtop XFCT applications. On the other hand, the detector with larger pixels coupled with a parallel-hole collimator is better suited for benchtop XFCT applications in which higher sensitivity and shorter scan time are essential.

Keywords

Monte Carlo simulations; Geant4; gold nanoparticles; x-ray fluorescence computed tomography; pixelated detectors; pinhole collimation; parallel-hole collimation

---

*Corresponding author: Sang Hyun Cho (scho@mdanderson.org).

1. Introduction

X-ray fluorescence computed tomography (XFCT) is a promising option for cancer molecular imaging when performed with bioconjugated high-atomic-number metal nanoparticles (NPs) such as gold NPs (GNPs) (Cheong et al., 2010). It utilizes x-ray fluorescence (XRF) photons emitted from these NPs irradiated with an external x-ray beam and therefore can detect and precisely map the NP distribution within the sample of interest. Whereas XFCT is traditionally performed with high-brilliance synchrotron x-ray sources (Boisseau, 1986; Boisseau et al., 1987; Rust et al., 1998), benchtop XFCT setups adopting diagnostic energy-range polychromatic x-ray sources have also been developed for imaging of GNPs (Cheong et al., 2010; Jones et al., 2012) and other metal probes (Kuang *et al.*, 2013a; Kuang *et al.*, 2013b).

The past decade has seen considerable advances in the development of benchtop XFCT techniques and systems. The performance of XFCT systems in terms of the sensitivity and image resolution has gradually improved through hardware and software optimization. For example, it was the key subject of early investigations to optimize the polychromatic x-ray source spectra and x-ray detection geometry for more efficient XRF production and detection (Jones et al., 2012; Manohar et al., 2014; Sjölin and Danielsson, 2014; Ahmad et al., 2015). In addition, investigators working on both synchrotron and benchtop XFCT have extensively studied detection configurations with pinhole collimators (pinhole detection configuration [PDC]) (Takeda *et al.,* 2009; Meng et al., 2011; Fu et al., 2013; Jiang et al., 2017; Jung et al., 2017; Sasaya et al., 2017) and parallel-hole collimators (parallel-hole detection configuration [PHDC]) (Cheong et al., 2010; Jones and Cho, 2011; Jones et al., 2012; Manohar et al., 2016; Ren et al., 2016; Manohar et al., 2018; Dunning and Bazalova-Carter, 2018) to further improve XFCT system sensitivity and image resolution while reducing delivered dose and scan time.

The PDC is a much sought-after configuration that has been the subject of numerous XRF imaging studies in recent years because of its capability in improving image quality. In fact, the millimeter-level XFCT image resolutions were first reported using this configuration, but the XFCT system suffered from very low sensitivity despite long scan time (Takeda *et al.,* 2009). In this configuration, severe restriction of the detector view by a collimator tends to weaken the sensitivity (Ishizu et al., 1995). Researchers have considered multipinhole collimator, similar to that used for single-photon emission computed tomography (Branderhorst et al., 2011), to address the aforementioned issue. The feasibility of the multipinhole detection configuration has been investigated using Monte Carlo (MC) simulations (Meng et al., 2011) and experimentally examined in XRF imaging of osmium-stained zebrafish and multiplex imaging of iron, zinc, and bromine solutions in a cylindrical plastic phantom (12-mm diameter) (Fu et al., 2013). Furthermore, a comparable system detected a low concentration of iodine in a relatively small (10-mm diameter) cylindrical plastic phantom, achieving submillimeter-level image resolution (Sasaya et al., 2017). Although the system performance enhancements in these investigations are noteworthy, an important point is that they were achieved with bright monochromatic/synchrotron x-ray sources using a pencil- or sheet-beam geometry within samples/phantoms smaller than 12

mm in diameter. Meanwhile, the feasibility of the PDC/multipinhole with polychromatic x-ray sources (sheet and fan beams) has also been investigated by MC simulations (Jung et al., 2017; Deng et al., 2018), experiments (Li et al., 2017), and analytic modeling (Tseng et al., 2019). Nonetheless, the question still remains open as to whether all of the anticipated benefits with PDC/multi-hole configurations can be realized in benchtop XFCT systems adopting cone beam sources, while satisfying the dose and scan time constraints for XFCT imaging of small animals or small animal-sized objects.

The PHDC also has been the subject of many benchtop XFCT studies because of its ability to improve XFCT system sensitivity. Since the first XFCT imaging of a GNP-loaded phantom using this detection configuration (in the form of a single-hole collimator with multiple detector translations) (Cheong et al., 2010), incident x-ray spectra and the PHDC have been optimized through a number of experimental and MC simulation studies. These efforts have led to notable system enhancements, enabling detection and imaging of biologically relevant concentrations of GNPs (<1 wt.%) within small animal-sized objects (Jones et al., 2011; Jones et al., 2012; Manohar et al., 2014; Ahmed et al., 2018; Manohar et al., 2018). Nevertheless, the current benchtop XFCT systems still suffer from long scan time, high imaging dose, and low image resolution when using the PHDC, partly due to the use of a single crystal (or pixel) detector, which requires multiple translations for scanning of an entire imaging object.

The feasibility of XFCT imaging (including direct XRF imaging/mapping) of GNP- or other NP-injected mice has already been demonstrated using the currently available benchtop XFCT systems incorporating the PHDC (Manohar et al., 2016) and PDC (Zhang et al., 2019; Jung et al., 2020). However, it is still challenging to detect and image sparsely distributed metal NPs at low concentrations (e.g., < ~0.1 wt.%) in small animals while keeping the dose and scan time within the practical limits. One way of addressing the sensitivity, image quality, dose, and scan time issues as described above is to make considerable modifications in the detection components of current benchtop XFCT systems by integrating array/pixelated detectors coupled with carefully designed collimators. Furthermore, it is crucial to understand the strengths and weaknesses of both the PDC and PHDC so that the adopted pixelated detectors can be used to their full potential. Thus, active research efforts are currently under way in this direction.

In the present work, we performed Geant4 MC simulations to investigate the feasibility of two different x-ray detection configurations for benchtop XFCT applications —one consisted of a detector with larger pixels (1mm x 1mm) (currently being developed) coupled to a parallel-hole collimator and the other made of a detector with submillimeter size pixels (0.25mm x 0.25mm) coupled to a pinhole collimator, resulting in a PHDC and a PDC respectively (Fig. 1). The former detector, which has been purposely designed to be used in a PHDC, would be excellent for achieving good XFCT sensitivity primarily due to large pixel size. Smaller pixels in the latter detector would be ideal in improving the image resolution when used in a PDC. The results of the current study explicitly demonstrated these expectations. They also provided insight into the strengths and weaknesses of both detection configurations, which will be valuable for further optimization of existing benchtop XFCT systems.

2. Methods

2.1 Monte Carlo Model

The MC model was developed using a Geant4 MC simulation toolkit (release 10.3; multithreaded) (Agostinelli *et al.,* 2003) as shown in Fig. 1(a). The model included an excitation component including x-ray generation, beam collimation, and filtration for irradiation of GNP-filled plastic phantoms, along with a detection component for the detection of XRF and scattered photons through detector collimators.

The excitation component was taken from our previous MC model (Ahmed et al., 2018), which consisted of a 125-kVp x-ray beam, a lead cone-beam collimator, and a 1.8-mm tin filter. Two 50-mm diameter plastic phantoms (large enough to be relevant to small animal imaging), were constructed to separately test the system's sensitivity (or GNP detection limit) and image resolution. First, the sensitivity phantom, shown in Fig. 1(b), consisted of five conically shaped regions with a height of 5 mm and upper and lower diameters of 10 mm and 0 mm, respectively. These regions were filled with GNP solutions of different concentrations (1.0, 0.7, 0.5, 0.3, and 0.1 wt.%). Consistent with our previous Monte Carlo simulation studies (Manohar et al., 2014; Ahmed et al., 2018), the GNP solutions were modelled as uniform mixtures of gold and water with different gold concentrations. Second, the resolution phantom, shown in Fig. 1(c), consisted of seven cylindrically shaped regions with a height of 5 mm and diameter of 2 mm that were filled with the 1 wt.% GNP solution but placed at varying radial distances. The distance from the x-ray source (tungsten target) to the center of both phantoms was fixed at 15 cm. These phantoms were aligned with the collimators and detectors as shown in Fig. 2.

The detection component in this model was composed of two different pixelated detectors and collimators capable of resolving the energy of photons reaching each pixel. The detectors were assumed to have an ideal energy resolution of 0.1 keV around gold K_a XRF peaks (~70 keV) with photon counting efficiency of 100%. The configuration adopting detector 1 (DC1), which is a PHDC ideally desired for high sensitivity, consisted of a detector with large (1 mm × 1 mm) pixels (0.2-mm septal thickness) coupled to a stainless steel parallel-hole collimator (0.9-mm hole diameter, 3.5-cm thickness). Another configuration with detector 2 (DC2), which is a PDC, consisted of a detector, comparable to that commercially available (Scuffham et al., 2012), which incorporated small (0.25 mm × 0.25 mm) pixels (0.2-mm septal thickness) coupled with a 5-mm-thick lead pinhole collimator with a 2-mm hole diameter and 60° acceptance angle. Both detectors were 55.0 mm x 11.0 mm in dimension and incorporated a total of 45 × 9 (detector 1) and 121 × 23 (detector 2) pixels. The feasibility of DC2 for imaging an area larger than the detector size was also tested by adjusting the collimator distance from the detector to 5.0 cm, 3.5 cm, and 2.0 cm, respectively producing effective magnifications of 1.0x, 0.7x, and 0.4x. The detectors in both configurations were placed at 90° with respect to the incident beam direction. Both collimators were placed 5 cm from the phantom's rotational axis. All system components were placed in air.

The interactions and transport of particles (photons and electrons) were modeled using the Penelope low-energy electromagnetic physics list that included photoelectric effects,

Compton scattering, and Rayleigh scattering for photon transport and multiple scattering, coulomb scattering, ionization, and bremsstrahlung x-ray production for electron transport (Baró et al., 1995). Particles with energy greater than 1 keV were tracked regardless of the material of passage.

All simulations were performed using a high-performance computing cluster at The University of Texas MD Anderson Cancer Center. The GNP-loaded phantoms were irradiated with a total of 2400 billion particles over 30 angular projections (12° increments) to obtain the XRF/scattered photon spectra. The simulation took about 8 h on average for 1 billion excitation particles using a computing node consisting of 23 central processing units (AMD 2.2- to 2.5-GHz quad-core processors).

2.2   XRF Signal Extraction and Image Reconstruction

Gold K-shell XRF signals (at gold K_α XRF photon energies of 67.0 and 68.8 keV) were extracted from acquired spectra by subtracting the average scattered photon counts in nearby energy bins. These XRF photon counts were added together to estimate the net XRF signal at each detector element. The net XRF signals were then used to generate sinograms or a projection data set (p). Therefore, each element in p (p_j) represented the XRF signal for one detector at a specific projection angle. This projection data set was used to reconstruct an image of corresponding phantoms with pixel element x_i by using the following equation:

$$p_j = \sum_i M_{i,j}\, x_i \tag{1}$$

where $M_{i,j}$ is the element of system matrix M, which represents the probability that the XRF signal is generated in a pixel x_i and detected in a projection element p_j. The linear attenuation coefficients, taken as *a priori* knowledge, were incorporated into this matrix.

With the initial (0th iteration) reconstructed image pixels x_i^0, the pixel distribution can be iteratively converged onto a likelihood source distribution (or image) by applying a maximum-likelihood expectation maximization (ML-EM) reconstruction algorithm (Shepp et al., 1982; Lange et al., 1984):

$$x_i^{m+1} = \frac{x_i^m}{\sum_j M_{i,j}} \times \sum_j M_{i,j} \frac{p_j}{\sum_j M_{i,j} x_i^m} \tag{2}$$

In this work, the ML-EM based image reconstruction scripts were written using MATLAB and implemented to reconstruct all sensitivity phantom images obtained using DC1 and DC2 along with resolution phantom images collected using DC2.

Conventionally, the system matrix used in an ML-EM image reconstruction algorithm assumes that the XRF photons from a pixel x_i are detected only by a projection element p_j directly along the axis of the detector collimator. This assumption may not always be accurate for the PHDC, as x_i can also remain in the line of sight of neighboring projection elements p_{j+1} and p_{j-1} as shown in Fig. 2. To address this issue, the detector's eye view (DEV)-based ordered subsets expectation maximization (OSEM) algorithm was developed by our group (Deng et al., 2019). This algorithm helps to improve the spatial resolution of

XFCT images under the PHDC. It uses the system matrix shown below, which is based on the original work by our group (Jones and Cho, 2011) but slightly modified to take into account the DEV effect:

$$M_{i,j} = \frac{d_{i,j}^2}{r_{i,j}^2} \exp\left(-\int_A^i \mu_b(l_i)dl_i\right) \exp\left(-\int_i^{C_j} \mu_g(l_{ij})dl_{ij}\right) \tag{3}$$

where $d_{i,j}$ is the width of the jth detector element; points A, i, and Cj are the beam entry, XRF production, and XRF exit points in the phantom, respectively; I_i is the distance between A and I, I_{ij} is the distance between i and Cj; $r_{i,j}$ is the distance between i and the detector element detecting XRF; μ_b and μ_g are the average attenuation coefficients of the phantom material at the intensity-weighted mean energy of excitation beam and gold K_a XRF photon energies, respectively. In the present work, this algorithm was used to reconstruct the resolution phantom images for DC1.

2.3   Analysis of Detection Limit, Image Resolution, Dose, and Scan Time

The detection limit per each pixel in the reconstructed images of the sensitivity phantom was estimated by using the method similar to that adopted in our previous study (Manohar et al., 2018). The GNP region and surrounding regions from the reconstructed images were used to calculate the mean signal and background values per pixel. The net XRF signal per pixel was then obtained by subtracting the mean background from the mean signal per pixel. The net XRF signal per pixel was plotted against its respective GNP concentration and the signal linearity was evaluated from the plot. By using the linear fit, the detection limit per pixel was found as the lowest GNP concentration at which the net XRF signal per pixel was more than two times the standard deviation of the background.

The reconstructed XFCT images of the resolution phantom and sensitivity phantom were analyzed for spatial resolution. The qualitative analysis of the spatial resolution in the reconstructed images were done via visual inspection. For quantitative analysis, the normalized signal intensities along the line joining centers of two consecutive GNP regions in the resolution phantom images were fitted with 2nd order Gaussian. Also, one-dimensional profiles of point spread function (PSF) were obtained. The full width at half maximum (FWHM) values for these PSFs were then calculated. For further analysis of spatial resolution, we evaluated the ratios of measured diameter of GNP region in the sensitivity phantom (estimated using the full width at tenth maximum for two-dimensional Gaussian fit of signal intensities in the reconstructed images) to the actual diameter of GNP region.

The absorbed dose at the isocenter was estimated from the total energy deposited at the dose scoring volume (5 mm diameter cylinder filled with water) placed at the center of the phantom. A total of 80 billion particles irradiated the phantom and the total energy deposited in the dose scoring volume by primary and secondary particles at each step were recorded, which was later converted into the absorbed dose (cGy). The Monte Carlo estimated dose was compared with the experimental dose rate at the isocenter of an experimental XFCT

system adopting the same irradiation geometry (Manohar et al., 2018) to estimate the scan time for a given number of incident particles.

3. Results

Calibration curves for the DC1 and DC2 (Fig. 3) were obtained by plotting mean pixel values for each GNP insert in reconstructed images of the sensitivity phantom against known GNP concentrations. This plot demonstrated a high degree of linearity ($R^2 > 0.99$) between GNP concentrations and XRF signal intensities. Thus, mean intensities of gold K_α peaks as determined using both detectors can be reliably used for quantification of GNP concentration. Also, according to this plot, the XRF signals from DC2, even under the optimal conditions of a 2-mm pinhole diameter and 1x magnification, were considerably weaker than the XRF signals from DC1 at every GNP concentration examined.

The overall performance of both detector configurations in terms of the system sensitivity is further highlighted in Figs. 4–6. The reconstructed axial and vertical cross-sectional images of the sensitivity phantom, obtained using DC1 (Fig. 4) and DC2 (Fig. 5), show clearly visible high-GNP-concentration regions. The XRF signal fell off sharply as the diameter of the GNP-containing region decreased, which was more prominent in the DC2. Furthermore, the net number of XRF photons scored by DC1 were about 16 times more than that scored by DC2 at all GNP concentrations. This suggests that DC1 was better than DC2 at detecting low concentrations of GNP solutions in the current phantoms

Fig. 6 shows the detection limit per detector pixel for both detection configurations, which depended on the sample size (diameter of GNP region). For very small GNP region (3 mm diameter), DC1 was at least twice as sensitive per detector pixel than was DC2. In this regard, DC1 performed consistently better for up to 6 mm-diameter GNP region, primarily because of greater detector pixel size. In such cases, Poisson noise may have dominated XRF photons scored by smaller pixels in DC2, making it less sensitive than DC1. Regardless, both configurations exhibited similar sensitivity per detector pixel at large diameters of GNP regions. Therefore, a detector with large pixels coupled with parallel-hole collimation would result in a PHDC that would be effective at detecting sparse distributions of GNPs/NPs within small animals.

As shown in reconstructed images in Fig.7, the spatial resolutions for DC2 deteriorated as the magnification decreased from 1.0x to 0.4x. However, the overall performance of this configuration at 1.0x and 0.7x in terms of image resolution was better compared to 0.4x magnification and also that of DC1. Although all four configurations (DC1, DC2 at 1.0x, 0.7x, and 0.4x magnifications) resolved the smallest insert separation (4.6 mm) in the resolution phantom, at 1.0x magnification, DC2 produced images with higher resolution than any other configurations tested. Of note, DC1 outperformed DC2 at 0.4x magnification and performed very close to it at 0.7x magnification in this regard. These results are also evident from the 1D profiles of PSF for GNP regions with smallest separation (4.6 mm) in the resolution phantom images and their estimated FWHM values as shown in Fig. 8. DC2 at 1.0x magnification also generated images with more accurate representation of diameters of GNP regions in the sensitivity phantom compared to other configurations, which was

noticeable with the lower ratios of measured to actual diameters of GNP regions in Fig. 9. Therefore, the PDC adopted in DC2 is desirable for improving the spatial resolution of XFCT images. Also, due to the large field of view at smaller magnifications, DC2 was able to image objects that are larger than the effective size of the detector. By applying the approach described in the preceding section, the absorbed dose at the isocenter of phantom was found to be 30.06 cGy, which was equivalent to the scan time of ~1.21 minutes (after a total of 2400 billion incident photons).

In summary, the XFCT system sensitivity was lower at smaller diameters of GNP regions than at larger ones regardless of the detection configuration. Owing to photon-counting statistics, the system sensitivity for a given size of GNP-loaded region can be improved by using a PHDC consisting of a detector with large pixels coupled with a parallel-hole collimator. On the other hand, the spatial resolution of XFCT images can be improved with a PDC consisting of a detector with submillimeter pixels paired with a pinhole collimator. However, low sensitivity of such PDC would be a problem in many benchtop XFCT applications. Finally, the estimated dose and scan time were less than those projected by a previous experimental study (Manohar et al. 2018).

4. Discussion

The primary aim of this study was to identify advantages and drawbacks of PHDC and PDC that utilized detector with large pixels and that with submillimeter pixels, respectively in benchtop XFCT applications. The obtained results elucidated a clear research direction to enhance the performance of benchtop XFCT systems, in terms of sensitivity and/or image resolution. Based on the current results, our PHDC will suffer from low image resolution. However, high sensitivity makes it a better choice for benchtop XFCT applications in which detection of sparsely distributed NPs within an imaging object is critical. On the other hand, the PDC simulated in this study is ideal for benchtop XFCT applications in which the image resolution is essential.

The commercial availability of pixelated detectors with submillimeter pixels (comparable to the one simulated in this work) provides an opportunity to experimentally test them with pinhole/parallel-hole collimators, possibly leading to clear delineation of the strengths and weaknesses of the resulting PDC and PHDC. Especially, such experimental testing efforts would determine the effects of important technical issues associated with pixelated detectors (e.g., charge sharing) which were not investigated in the current MC study. In PDC, most of the scattered photons are blocked by the collimator, which helps reduce the noise and improve the image quality. However, this also prevents the bulk of XRF photons from reaching the detector, thereby worsening the XFCT system sensitivity. Although the inclusion of a detector with larger pixels into such a PDC may seem as a viable alternative, the aforesaid restrictions imposed by the collimator will prevent it from achieving better sensitivity. Accordingly, meticulously designed multi-pinhole collimators may provide an option for enhancing the performance of pinhole-based XFCT systems.

In principle, adoption of a detector with submillimeter pixels and a collimator with comparably sized holes is one way of improving the image resolution in the PHDC.

However, such a collimator would not only be difficult to fabricate but also negatively impact the XFCT system sensitivity. It is worth noting that achieving submillimeter image resolutions may not be necessary in many benchtop XFCT applications, as the role of XFCT is primarily to reveal functional and/or molecular characteristics of imaged objects (rather than providing anatomical details). Especially, this is well-justified within the context of multimodal imaging (transmission CT and XFCT), which is highlighted in the literature (Manohar et al., 2016; Manohar et al., 2018). Considering the aspects described above, the use of a parallel-hole collimator with an aperture size larger than the individual pixel size in the detector can be an acceptable compromise for improving the overall performance of benchtop XFCT systems. We are currently testing this approach.

The MC simulation work presented here provided an estimation of the scan time (or dose) in experimental work involving the exact same PDC and PHDC. As expected, the fact that each collimator hole in PHDC acts as a single projection resulted in an overall reduction in the scan time when PHDC is used. For example, 45×9 collimator holes in the parallel-hole collimator with a matching pixelated detector would result in approximately 405 times reduction in scan time, compared to a single-hole collimator coupled with a single crystal/pixel detector, while scanning a three dimensional object of the size no larger than the size of the pixelated detector. For PDC, however, the lack of any experimental work involving the exact PDC used in this MC simulation makes it difficult to provide any meaningful comparison or projection at this time.

5. Conclusion

In the current MC study, we examined the effects of detector pixel size and collimator design on the performance of two benchtop XFCT systems in terms of sensitivity and image resolution. Between the two detection configurations simulated in this study, the PHDC demonstrated better sensitivity than the PDC and could be more desirable for detecting the scant distribution of NPs in small animal-sized objects. The PDC, on the other hand, would be more appropriate for producing high resolution XFCT images. Another advantage of PDC is that one can utilize the magnification to facilitate imaging of objects larger than the field of view of the detector with minimal degradation in image quality. The PDC investigated in this study, however, was found less sensitive than the PHDC. Therefore, it might be necessary to make changes in the collimator (e.g., use of multi-pinhole) or increase the scan time to improve its sensitivity. Overall, for benchtop XFCT applications in which higher sensitivity (lower detection limit) and short scan time are essential, the PHDC can be a better choice than the PDC.

Acknowledgements

References

Agostinelli S et al. 2003 GEANT4—a simulation toolkit Nucl. Instrum. Methods Phys. Res. Section A: Accelerators, Spectrometers, Detectors and Associated Equipment 506 250–303

Ahmad M, Bazalova-Carter M, Fahrig R and Xing L 2015 Optimized Detector Angular Configuration Increases the Sensitivity of X-ray Fluorescence Computed Tomography (XFCT) IEEE Trans. Med. Imaging 34 1140–1147 [PubMed: 25474808]

Ahmed M F, Yasar S and Cho S H 2018 A Monte Carlo Model of a Benchtop X-Ray Fluorescence Computed Tomography System and Its Application to Validate a Deconvolution-based X-Ray Fluorescence Signal Extraction Method IEEE Trans. Med. Imaging 37 2483–2492. [PubMed: 29994762]

Baró J, Sempau J, Fernández-Varea J M and Salvat F 1995 PENELOPE: An algorithm for Monte Carlo simulation of the penetration and energy loss of electrons and positrons in matter Nucl. Instrum. Methods Phys. Res. Section B: Beam Interactions with Materials and Atoms 100 31–46

Boisseau P 1986 Determination of Three Dimensional Trace Element Distributions by the Use of Monochromatic X-ray Microbeams. Cambridge, MA: Massachusetts Institute of Technology, Department of Physics

Boisseau P and Grodzins L 1987 Fluorescence Tomography Using Synchrotron Radiation at the Nsls Hyperfine Interact. 33 283–292

Branderhorst W, Vastenhouw B, van der Have F, Blezer E L, Bleeker W K and Beekman F J 2011 Targeted multi-pinhole SPECT Eur. J. Nucl. Med. Mol. I 38 552–561

Cheong S K, Jones B L, Siddiqi A K, Liu F, Manohar N and Cho S H 2010 X-ray fluorescence computed tomography (XFCT) imaging of gold nanoparticle-loaded objects using 110 kVp x-rays Phys. Med. Biol 55 647 [PubMed: 20071757]

Deng L, Wei B, He P, Zhang Y and Feng P 2018 A Geant4-based Monte Carlo study of a benchtop multi-pinhole X-ray fluorescence computed tomography imaging Int. J. Nanomedicine 13 7207–7216 [PubMed: 30510413]

Deng L, Ahmed M F, Jayarathna S, Feng P, Wei B and Cho S H 2019 Note: A detector's eye view (DEV)-based OSEM algorithm for benchtop x-ray fluorescence computed tomography (XFCT) image reconstruction Phys. Med. Biol 64 NT02

Dunning CAS and Bazalova-Carter M 2018 Sheet beam x-ray fluorescence computed tomography (XFCT) imaging of gold nanoparticles. Med. Phys 45–2582 [PubMed: 30372521]

Fu G, Meng L J, Eng P, Newville M, Vargas P and La Riviere P 2013 Experimental demonstration of novel imaging geometries for x-ray fluorescence computed tomography Med. Phys 40 061903 [PubMed: 23718594]

Ishizu K et al. 1995 Ultra-high Resolution SPECT System Using Four Pinhole Collimators for Small Animal Studies J. Nucl. Med 36 2282–2287 [PubMed: 8523120]

Jiang S, He P, Deng L, Chen M and Wei B 2017 Monte Carlo Simulation for Polychromatic X-ray Fluorescence Computed Tomography with Sheet-Beam Geometry Int. J. Biomed. Imaging 2017 7916260 [PubMed: 28567054]

Jones B L and Cho S H 2011 The feasibility of polychromatic cone-beam x-ray fluorescence computed tomography (XFCT) imaging of gold nanoparticle-loaded objects: a Monte Carlo study Phys. Med. Biol 56 3719 [PubMed: 21628767]

Jones B L, Manohar N, Reynoso F, Karellas A and Cho S H 2012 Experimental demonstration of benchtop x-ray fluorescence computed tomography (XFCT) of gold nanoparticle-loaded objects using lead- and tin-filtered polychromatic cone-beams Phys. Med. Biol 57 N457 [PubMed: 23135315]

Jung S, Sung W and Ye S J 2017 Pinhole X-ray fluorescence imaging of gadolinium and gold nanoparticles using polychromatic X-rays: a Monte Carlo study Int. J. Nanomed 12 5805–5817

Jung S et al. 2020 Dynamic in vivo X-ray Fluorescence Imaging of Gold in Living Mice Exposed to Gold Nanoparticles IEEE Trans. Med. Imaging 39 526–33 [PubMed: 31380749]

Kuang Y, Pratx G, Bazalova M, Meng B, Qian J and Xing L 2013a First demonstration of multiplexed x-ray fluorescence computed tomography (XFCT) imaging IEEE Trans. Med. Imaging 32 262–7 [PubMed: 23076031]

Kuang Y, Pratx G, Bazalova M, Qian J, Meng B and Xing L 2013b Development of XFCT imaging strategy for monitoring the spatial distribution of platinum-based chemodrugs: instrumentation and phantom validation Med. Phys 40 030701 [PubMed: 23464279]

Lange K and Carson R 1984 Em Reconstruction Algorithms for Emission and Transmission Tomography J. Comput. Assist. Tomogr 8 306–316 [PubMed: 6608535]

Li L, Zhang S, Li R and Chen Z 2017 Full-field fan-beam x-ray fluorescence computed tomography with a conventional x-ray tybe and photon-counting detectors for fast nanoparticle bioimaging Opt. Eng 56 043106

Manohar N, Jones B L and Cho S H 2014 Improving x-ray fluorescence signal for benchtop polychromatic cone-beam x-ray fluorescence computed tomography by incident x-ray spectrum optimization: A Monte Carlo study Med. Phys 41 101906 [PubMed: 25281958]

Manohar N, Reynoso F J, Diagaradjane P, Krishnan S and Cho S H 2016 Quantitative imaging of gold nanoparticle distribution in a tumor-bearing mouse using benchtop x-ray fluorescence computed tomography Sci. Rep 6 22079 [PubMed: 26912068]

Manohar N, Reynoso F J and Cho S H 2018 Technical Note: A benchtop cone-beam x-ray fluorescence computed tomography (XFCT) system with a high-power x-ray source and transmission CT imaging capability Med. Phys 45 4652–4659 [PubMed: 30125950]

Meng L J, Li N and La Riviere P J 2011 X-Ray Fluorescence Emission Tomography (XFET) With Novel Imaging Geometries-A Monte Carlo Study IEEE Trans. Nucl. Sci 58 3359–3369 [PubMed: 22228913]

Ren L, Wu D, Li Y, Chen W R, Zheng B and Liu H 2016 Optimized acquisition time for x-ray fluorescence imaging og gold nanoparticle: a preliminary study using photon counting detector Proc. SPIE Biophotonics and Immune Response XI 9709 97090P

Rust G and Weigelt J 1998 X-ray fluorescent computer tomography with synchrotron radiation IEEE Trans. Nucl. Sci 45 75–88

Sasaya T, Sunaguchi N, Hyodo K, Zeniya T and Yuasa T 2017 Multi-pinhole fluorescent x-ray computed tomography for molecular imaging Sci. Rep 7 5742 [PubMed: 28720758]

Scuffham J W, Wilson M D, Seller P, Veale M C, Sellin P J, Jacques S D M and Cernik R J 2012 A CdTe detector for hyperspectral SPECT imaging J. Instrum 7 08027

Shepp L A and Vardi Y 1982 Maximum likelihood reconstruction for emission tomography IEEE Trans. Med. Imaging 1 113–22 [PubMed: 18238264]

Sjölin M and Danielsson M 2014 Improved signal-to-noise ratio for non-perpendicular detection angles in x-ray fluorescence computed tomography (XFCT). Phys Med Biol. 59 6507 [PubMed: 25310695]

Takeda T et al. 2009 X-ray fluorescent CT imaging of cerebral uptake of stable-iodine perfusion agent iodoamphetamine analog IMP in mice J. Synchrotron Radiat 16 57–62 [PubMed: 19096175]

Tseng H W, Vedantham S, Cho S H and Karellas A 2019 Joint optimization of collimator and reconstruction parameters in x-ray fluorescence computed tomography using analytical point spread function and model observer IEEE Trans. Biomed. Eng doi: 10.1109/TBME.2019.2963040.

Zhang S Y, Li L, Chen J Y, Chen Z Q, Zhang W L and Lu H B 2019 Quantitative Imaging of Gd Nanoparticles in Mice Using Benchtop Cone-Beam X-ray Fluorescence Computed Tomography System Int. J. Mol. Sci 20 2315
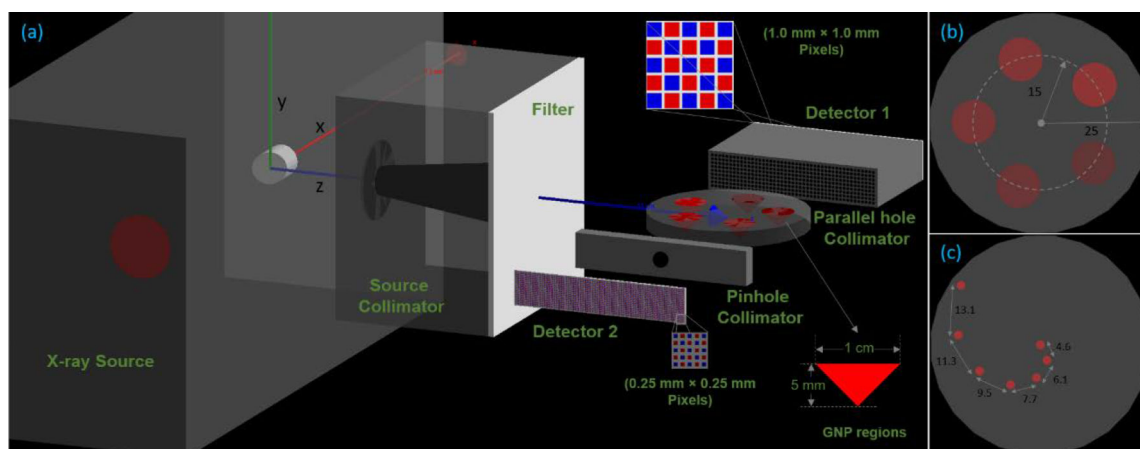
Fig. 1.
Geant4 MC simulation geometry. (a) Irradiation and detection setup. (b) Sensitivity phantom with five conically shaped regions. (c) Resolution phantom with seven cylindrical regions. Collimators were placed 5 cm from the center of both phantoms.
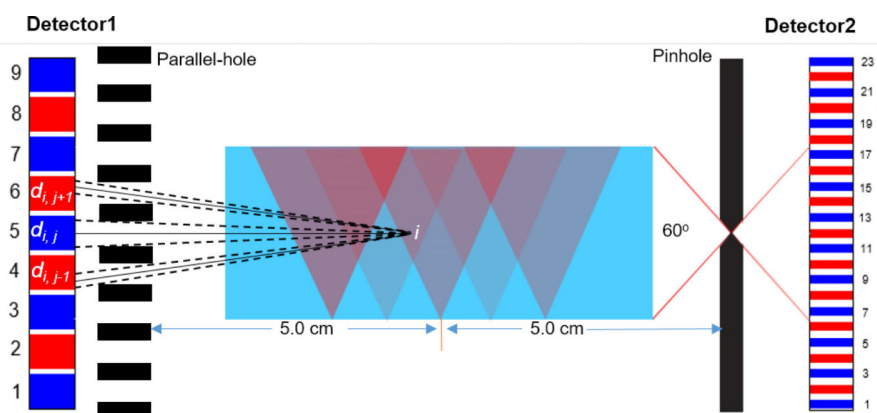
Fig. 2.
Cross sectional view of the two detection configurations and phantom setup (only the sensitivity phantom is shown). The DEV of the XRF production point *i* is depicted by dotted lines. The pixel arrangements (vertical) in both detectors are represented by blue and red regions with white septa. This figure is for illustrative purposes only and is not drawn to scale.
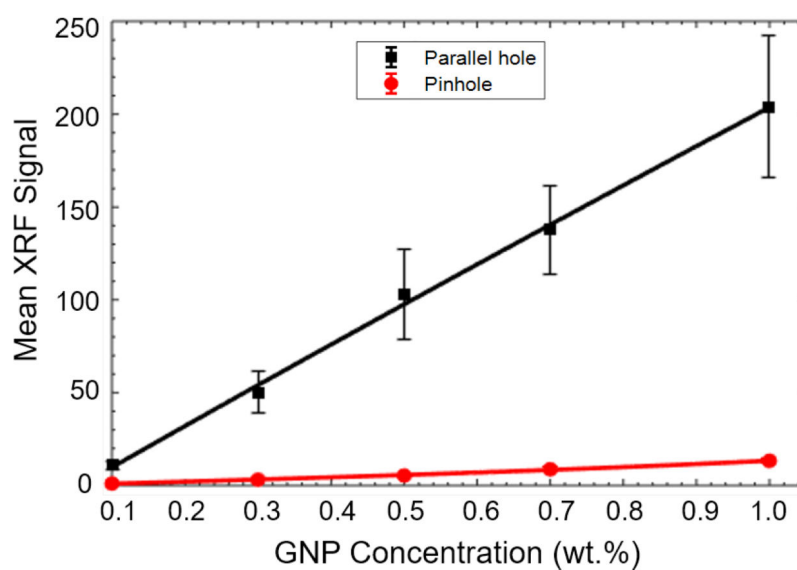
Fig. 3.
Calibration curves showing the mean XRF signals per pixel from GNP regions within the sensitivity phantom as a function of GNP concentration for the two detection configurations. The standard deviations associated with pinhole configuration data were smaller than the size of data symbols.
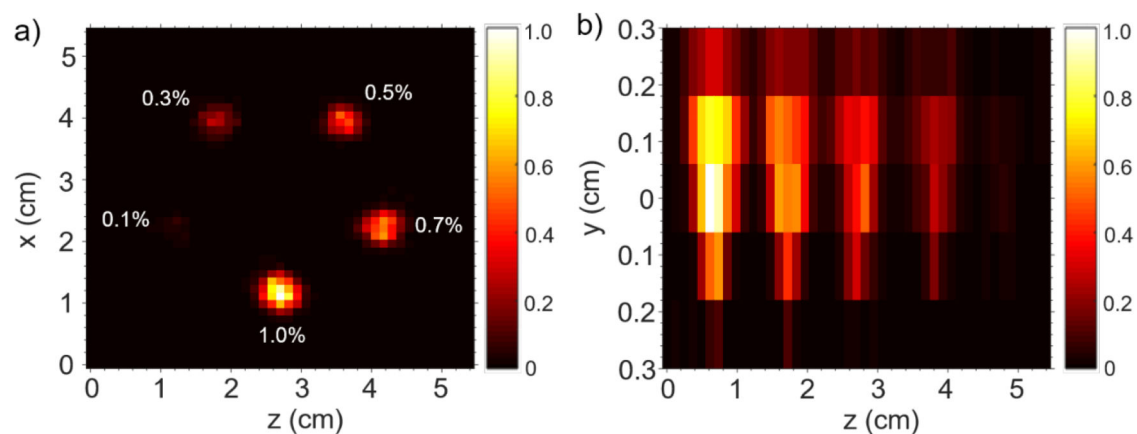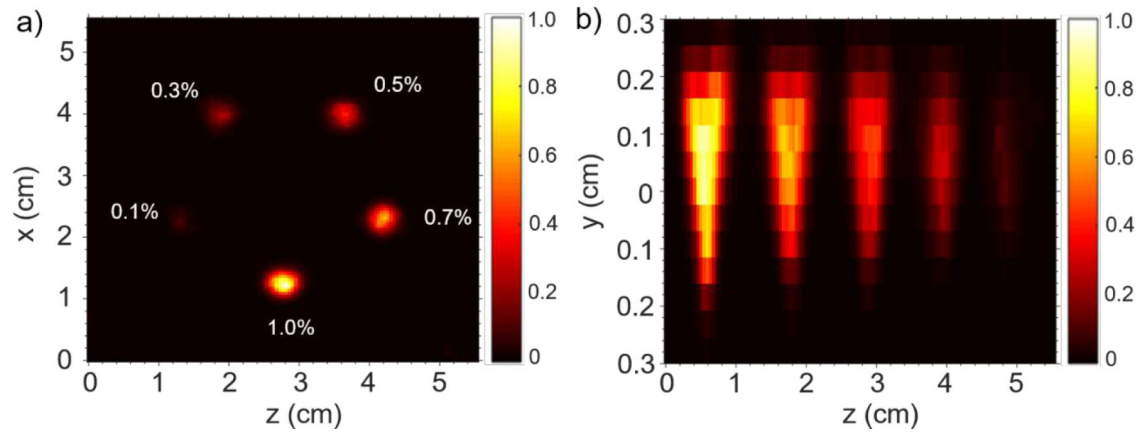
Fig. 4.
(a) Reconstructed image of central-horizontal (y=0, phantom center) plane of the sensitivity phantom showing different concentrations of GNP regions. (b) Superimposed image of vertical or x-planes (passing through the center of each GNP region) obtained using the DC1. The color bar represents the GNP concentration by wt. %.
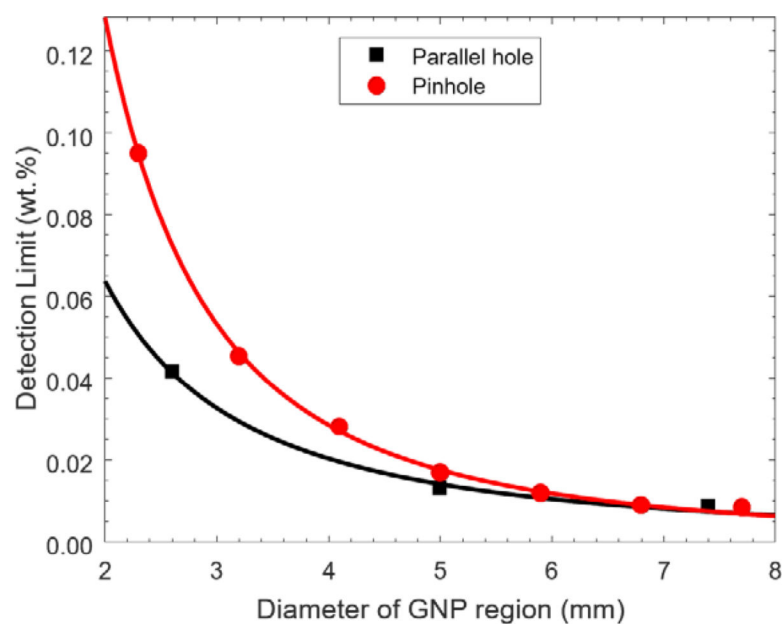
Fig. 5.
(a) Reconstructed image of central-horizontal (y=0, phantom center) plane of the sensitivity phantom showing different concentrations of GNP regions. (b) Superimposed image of vertical or x-planes (passing through the center of each GNP region) obtained using the DC2. The color bar represents the GNP concentration by wt. %.

Fig. 6.
Detection limit per pixel (with 95% confidence interval) for DC1 and DC2 estimated at different diameter of GNP region.
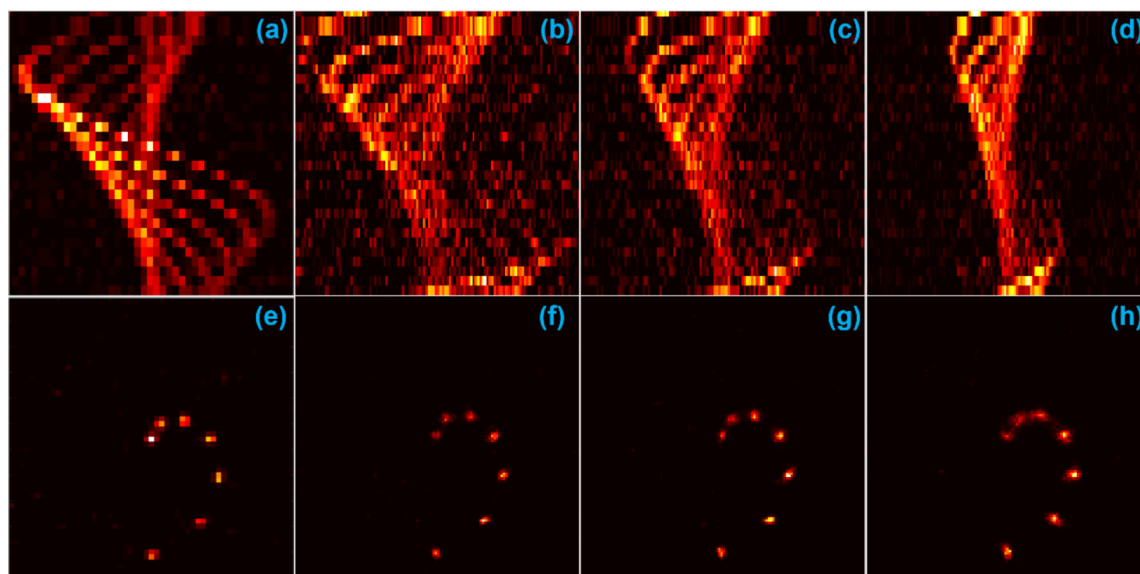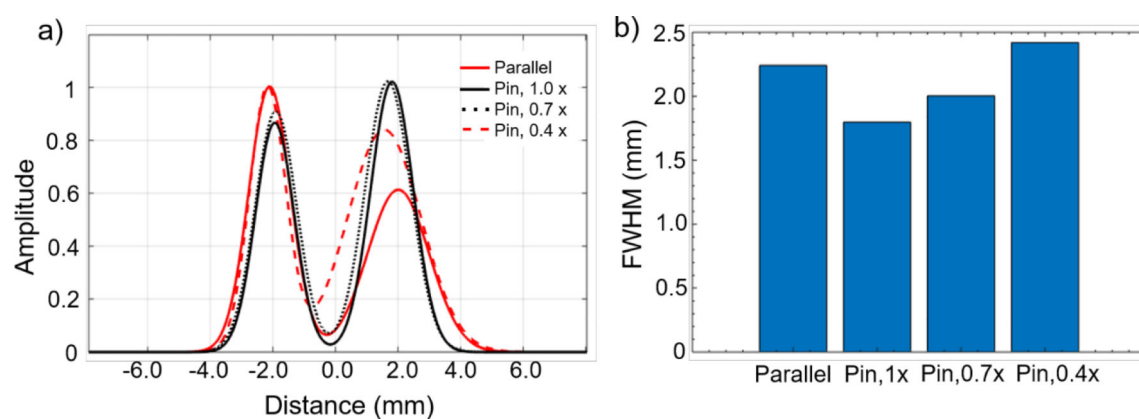
Fig. 7.
Sinograms (projection data set) for the spatial resolution phantom obtained using DC1 (a) and DC2 at magnifications of 1.0x (b), 0.7x (c), and 0.4x (d). The bottom panel shows images of horizontal slice of the same phantom that were reconstructed using the DEV-based OSEM algorithm for DC1 (e) and the ML-EM algorithm for DC2 at the respective magnifications (f-h).

Fig. 8.
(a) The 1D profiles of PSF obtained by fitting (with 2nd order Gaussian) normalized signal intensities (data points not shown) along the line joining centers of two consecutive GNP regions. Figure shows only the profiles of PSF for GNP regions with smallest separation (4.6 mm) in the resolution phantom images obtained using DC1 and DC2 at different magnifications. (b) Figure shows the average FWHM of PSFs for respective configurations.
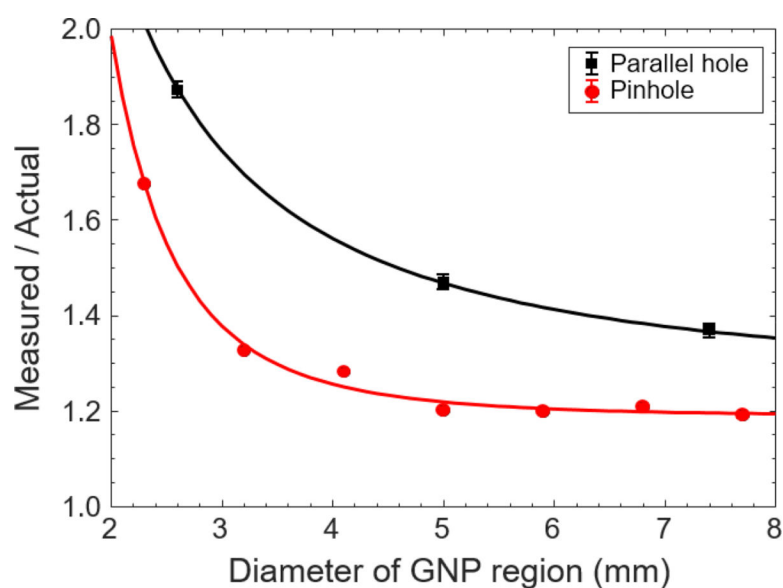
Fig. 9.
Plot of the ratios of measured diameters of GNP regions (full width at tenth maximum values of two-dimensional Gaussian fit of measured signal intensities) to actual diameters of GNP regions in the sensitivity phantom. The standard deviations for pinhole data were smaller than the size of data symbols.